



Construction of porous CoTiO₃ microrods with enhanced performance as lithium-ion battery anode



Meng Sun^a, Xiaoli Sheng^a, Sijie Li^a, Zhipeng Cui^a, Tao Li^b, Qingye Zhang^a, Fei Xie^a,
Yiqian Wang^{a,*}

^a College of Physics, Qingdao University, No. 308 Ningxia Road, Qingdao 266071, People's Republic of China

^b College of Textile & Clothing, Qingdao University, No. 308 Ningxia Road, Qingdao 266071, People's Republic of China

ARTICLE INFO

Article history:

Received 19 April 2022

Received in revised form 4 August 2022

Accepted 14 August 2022

Available online 19 August 2022

Keywords:

CTO MRs

CTO NPs

Porous structure

LIBs

Electrochemical performance

ABSTRACT

CoTiO₃ microrods (CTO MRs) and CoTiO₃ nanoparticles (CTO NPs) were successfully prepared by a solvothermal method followed by thermal annealing in air. The correlation between structure and electrochemical properties of both CTO NPs and CTO MRs was studied by a series of material analysis and characterizations, as well as electrochemical tests. When used as anode materials for lithium-ion batteries (LIBs), CTO MRs exhibit a higher discharge capacity (410 mAh g⁻¹ at 100 mA g⁻¹ after 200 cycles) and better rate capability, compared with those of CTO NPs. The enhanced electrochemical properties of CTO MRs can be attributed to good Li⁺ diffusion ability, large specific surface area and porous rod-like structure composed of a large number of NPs. This work provides a feasible strategy to develop a promising material with improved performance as anode for LIBs.

© 2022 Elsevier B.V. All rights reserved.

1. Introduction

Energy storage is still the common bottleneck of renewable energy technologies, as well as the holy grail for the electrification of transports. Among various storage devices, lithium-ion batteries (LIBs) have played an important role as they possess a high energy density, a long lifetime and environmental friendliness. LIBs have been widely employed in mobile phones, portable computers, electric vehicles and so on [1–4].

When LIBs were first commercialized in the 1990s, LiCoO₂ and graphite were used as the cathode and anode materials, respectively [5]. The graphite anode is still in use in most commercial LIBs [6]. However, its low theoretical capacity (372 mAh g⁻¹) severely hinders the achievement of high energy density for next generation LIBs [7,8]. Because of the slow kinetics and size dependent effect during the charge–discharge process for the commercial graphite electrode, the demand for rapid charging of LIBs cannot be met, and the rate performance at high current densities is poor. Over the past two decades, transition metal oxides have been considered as potential candidates to replace traditional graphite anode materials due to their high capacity, environmental friendliness, and low cost [9–12]. Compared with single transition metal oxides, mixed transition

metal oxides show better electrochemical performance in the application of anode materials due to the advantages of diversity and complementarity [13–16]. Recently, researchers have found that some bimetallic titanates, especially CoTiO₃ nanostructures, show excellent cycling performance and a superior lithium storage capacity [17]. According to the lithium storage mechanism (CoTiO₃ + 3Li⁺ + 3e⁻ ↔ LiTiO₂ + Co + Li₂O), the theoretical specific capacity of CoTiO₃ is 519.5 mAh g⁻¹, suggesting that it is a great potential anode material for LIBs. Nevertheless, low electrical conductivity coupled with the structural damage during the charge–discharge process resulted in a rapid capacity fading and inferior cycling performance of CoTiO₃. The electrochemical properties of the electrode materials are associated with their microscopic structure. Thus, the preparation of different microstructures for transition metal oxides is beneficial for the improvement of their cycling stability and rate capability during electrochemical processes.

Herein, CoTiO₃ microrods (CTO MRs) and CoTiO₃ nanoparticles (CTO NPs) were synthesized by a simple solvothermal method and used as anode materials in LIBs. In addition, the structural and electrochemical properties of CTO MRs and CTO NPs were systematically investigated. CTO MRs deliver better reversible capacity and rate performance. The CTO MRs as the anode material for LIBs show greatly enhanced electrochemical performances compared to that of CTO NPs. This enhancement is mainly attributed to the porous rod-like structure, which provides more additional space for lithium-ion

* Corresponding author.

E-mail address: yqwang@qdu.edu.cn (Y. Wang).

storage during the repeated Li⁺ insertion/extraction process, and simultaneously improves the kinetic diffusion of lithium ions/electrons.

2. Experimental

2.1. Materials synthesis

All chemicals were of analytical grade and were used as received without further purification. CTO MRs and CTO NPs were synthesized by a facile hydrothermal process followed by thermal annealing in air. In a typical procedure, stoichiometric amounts of cobalt acetate tetrahydrate, tetrabutyl titanate and urea were successively dissolved in a molar ratio of 1:1: 3 into 60 mL ethylene glycol (EG) to form a clear red solution under magnetic stirring at room temperature. Subsequently, the mixed solution was stirred for 3 h and then transferred into a 100 mL Teflon-sealed autoclave and maintained at 180 °C for 6 h to obtain the precursor. After the autoclave was cooled to room temperature, the resulting precipitates were collected by centrifugation, washed several times with distilled water and ethanol, then dried at 60 °C overnight. The resulting precursor was calcined at 650 °C in air for 3 h at a heating rate of 4 °C/min. Finally, CTO MRs green powder was obtained. We also prepared CTO NPs using the same procedure. The only difference is that the solvent changes from ethylene glycol to absolute ethanol.

2.2. Materials characterization

Thermogravimetric analysis (TGA) was conducted using a Netzsch TG 209 apparatus under an air flow from room temperature to 900 °C at a heating rate of 10 °C/min. X-ray diffraction (XRD) patterns were acquired using a SmartLab XRD diffractometer with Cu-K α_1 radiation ($\lambda = 1.5406 \text{ \AA}$). Raman spectra were recorded on a RM 2000 microscopic confocal Raman spectrometer (Renishaw PLC, England) using a 514-nm laser line for the excitation. The morphology of the samples was characterized by scanning electron microscopy (SEM, Hitachi S-4800). Bright-field (BF) images, high-resolution transmission electron microscopy (HRTEM) images and selected-area electron diffraction (SAED) patterns were obtained using a JEOL JEM2100F transmission electron microscope (TEM) with an accelerating voltage of 200 kV. Nitrogen adsorption-desorption tests were carried out on an automatic volumetric sorption analyzer (NOVA 1100, Quantachrome, USA) at 77 K. The Brunauer-Emmett-Teller (BET) method was used to calculate the specific surface areas of samples. The Barrett-Joyner-Halenda (BJH) method was used to determine the pore size distributions from the adsorption branches of the isotherms.

2.3. Electrochemical measurements

CR2025-type coin cells were assembled in a high-purity argon-filled glove box, where the moisture and oxygen concentration are less than 0.1 ppm, using a lithium foil as counter electrode. The anodes were prepared by mixing the active material (CTO MRs, and CTO NPs), carbon black and polyvinylidene fluoride (PVDF) in a weight ratio of 70:20:10 (wt%) onto a pure copper foil. N-methylpyrrolidone (NMP) was used as solvent. The electrolyte was composed of 1 M LiPF₆ solution of ethylene carbonate (EC)/dimethyl carbonate (DMC)/diethyl carbonate (DEC) (1:1:1 in volume). The electrochemical performance was tested on a LAND CT2001 battery test system in the 0.01 V to 3.00 V voltage range at room temperature. Cyclic voltammetry (CV) measurements (over the potential range from 0.01–3.00 V at a scan rate of 0.3 mV s⁻¹) and electrochemical impedance spectroscopy (EIS) tests were performed on a Metrohm Autolab electrochemical workstation (PGSTAT 302) at the 100 kHz to 0.01 Hz frequency range with a disturbance amplitude of 5 mV.

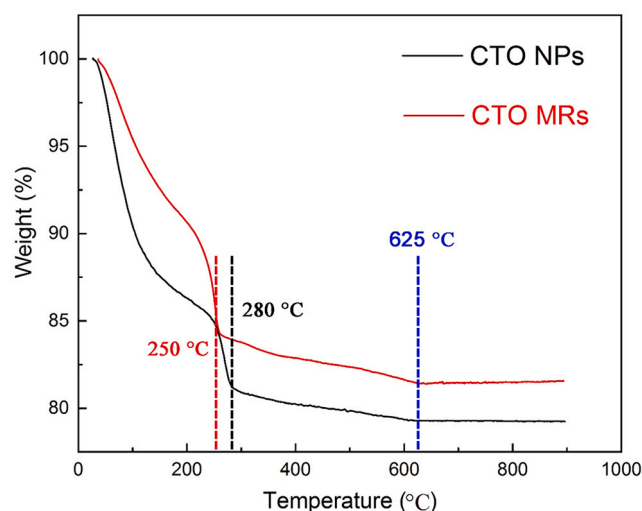


Fig. 1. TGA curve of CTO MRs and CTO NPs precursors.

3. Results and discussion

TGA measurements were initially performed to assess the follow-up calcination process of as-prepared precursors (presented in Fig. 1a). TGA curves of both CTO NPs and CTO MRs precursors can be divided into three stages: rapid decline, slow decline and stabilization stage. For CTO NPs precursor, the observed weight loss below 280 °C is attributed to the evaporation of adsorbed water; the weight loss between 280 °C and 625 °C results from the decomposition of carbon-containing organic matter; no weight loss was observed beyond 625 °C. The TGA curve of CTO MRs precursor is similar to that of CTO NPs precursor. The obvious difference is the decomposition temperature of carbon-containing organic matter in the precursors of CTO NPs (280 °C) and CTO MRs (250 °C). The TGA curves of both precursors do not show any obvious weight loss above 625 °C, indicating that there is no additional phase or structural change. Therefore, 650 °C is chosen as the annealing temperature to obtain the CTO with high purity.

Fig. 2 shows the XRD patterns of CTO MRs and CTO NPs. All the diffraction peaks can be well assigned to the rhombohedral CTO phase [JCPDS no.: 72-1069] [18,19]. No characteristic peaks of other impurities such as TiO₂, CoO, and Co₃O₄ were detected, indicating

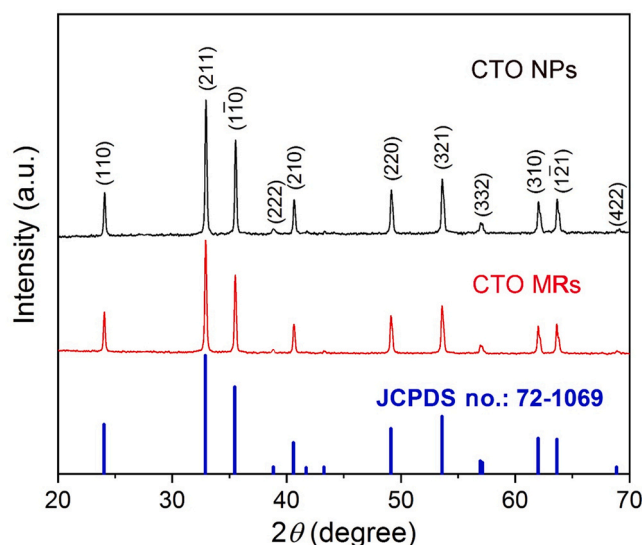


Fig. 2. XRD patterns of CTO MRs and CTO NPs.

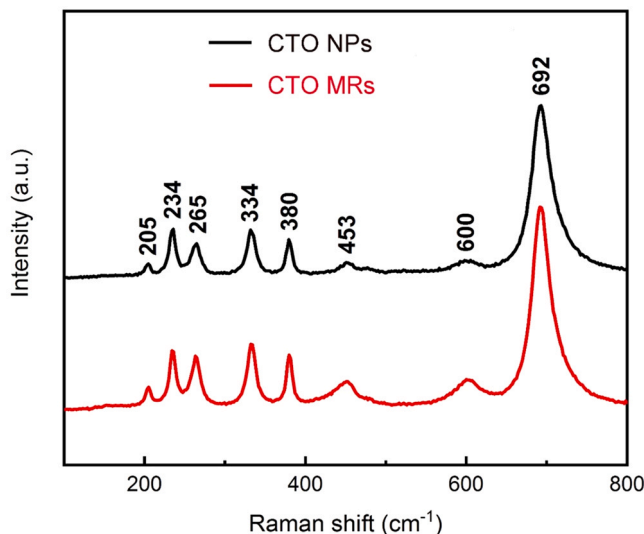


Fig. 3. Raman spectra of CTO NPs and CTO MRs.

that both CTO MRs and CTO NPs have high purity. The sharp diffraction peaks indicate that CTO MRs and CTO NPs are highly crystalline. Careful comparison of the XRD patterns shows that the diffraction peak of CTO MRs is sharper, which is due to the fact that the overall size of the CTO MRs is larger than that of the CTO NPs.

Raman investigations of CTO NPs and CTO MRs were conducted, as shown in Fig. 3. All Raman modes from CTO NPs and CTO MRs (absorption at 692, 600, 453, 380, 334, 265, 234 and 205 cm^{-1}) are consistent with previous studies [20,21]. The most intense Raman mode at 692 cm^{-1} arises from the highest frequency vibrational mode of CoO_6 octahedra that is the symmetric stretching mode [20,21]. No additional bands could be found in the Raman spectrum, which further confirms that both as-prepared products are pure CTO.

The morphologies of CTO NPs and CTO MRs were investigated by SEM. Fig. 4a and b display SEM images of CTO NPs and CTO MRs, respectively. Analysis of the micrographs shows that CTO NPs have an average size of ~ 70 nm, whereas the surface of CTO MRs exhibits numerous pores. The average length and width of CTO MRs are measured to be 1.85 μm and 345 nm, respectively.

To obtain the microstructure information of CTO NPs and CTO MRs in detail, TEM characterization was performed (Fig. 5 and Fig. 6). Fig. 5a shows a typical BF TEM image of CTO NPs. The prepared CTO NPs appear to have uniform size and good dispersion. The SAED patterns (Fig. 5a) can be indexed to rhombohedral CTO, consistent with the results obtained from XRD patterns. The six diffraction rings from the center to the outside correspond to the (110),

(211), ($1\bar{1}0$), (222), (210) and (220) planes of CTO, respectively, indicating that CTO NPs are polycrystalline. Fig. 5b shows the statistical size distribution for CTO NPs with an average size of 69 nm. Fig. 5c displays an HRTEM image of an individual CTO nanoparticle, showing that the outer surfaces are composed of several small facets, corresponding to the (222), (210), (012), (210), and (222) planes of the rhombohedral phase CTO, respectively. Fig. 5d shows an enlarged HRTEM image of the regions enclosed by white rectangles in (c). The lattice spacings in Fig. 5d are measured to be 2.32 Å, 2.22 Å and 2.22 Å, corresponding to the (222), (210) and (012) planar spacings of CTO, respectively. To our knowledge, such CTO NPs with a regular shape have not been reported in previous studies.

Fig. 6a and b display BF TEM images of CTO MRs. CTO MRs exhibit a rod morphology and uniform size. Fig. 6c and d show the statistical distribution of the length and width of CTO MRs. The average length and width of CTO MRs were 1.85 μm and 345 nm, respectively. Fig. 7a, b and c show the BF TEM images of CTO MRs. The CTO MRs are observed to be composed of numerous small nanoparticles, and some small particles are marked with red dotted lines. By counting the size of 100 particles on CTO MRs, the statistical size distribution of the particles on CTO MRs was obtained. The average size was about 55 nm, as shown in Fig. 7d. It can be concluded that the nanoparticles on CTO MRs have smaller sizes than CTO NPs.

Fig. 8a shows BF TEM image of CTO MRs. The CTO MRs are composed of submicron rods with uniform size. The SAED pattern can be labeled as a rhombohedral phase CTO, consistent with the XRD results. The four diffraction rings from the center to the outside correspond to the (110), (211), ($1\bar{1}0$), and (210) planes of CTO, respectively, indicating that CTO MRs are polycrystalline. Fig. 8b displays the TEM images of the two crossing rods. The two rods have a similar size, and their length and width are approximately 1.4 μm and 200 nm, respectively. Moreover, a large number of holes are observed on the surface of the CTO MRs, which is consistent with SEM results. This porous structure helps to buffer volume expansion and maintain the structural stability of CTO MRs during electrochemical cycling. Fig. 8c displays an enlarged HRTEM image of the regions enclosed by red rectangles in (b). To clearly observe the lattice of CTO MRs, the white rectangular region in (c) was further enlarged, as shown in Fig. 8d. The lattice spacings are measured to be 2.72 Å, 2.53 Å and 2.72 Å, corresponding to the (211), ($1\bar{1}0$) and (121) planes of the rhombohedral CTO, respectively. Such a porous structure can provide an effective channel for sufficient penetration of the electrolyte in the CTO MRs electrode to realize the high-speed transport of Li^+ .

The specific surface area and pore size of CTO NPs and CTO MRs were measured by nitrogen adsorption and desorption tests. Fig. 9a shows the type-IV adsorption/desorption isotherms with a hysteresis loop, indicating that both CTO NPs and CTO MRs have a mesoporous structure [22–24]. The pore size distribution curves in Fig. 9b and c illustrate that CTO NPs and CTO MRs have a predominant

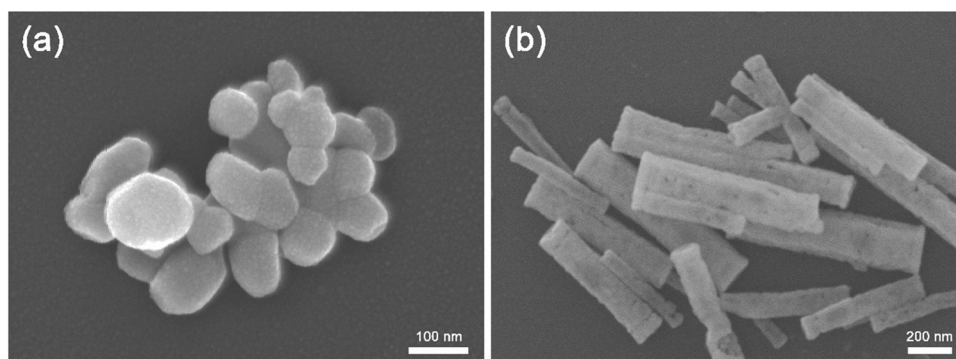


Fig. 4. SEM images of CTO NPs (a) and CTO MRs (b).

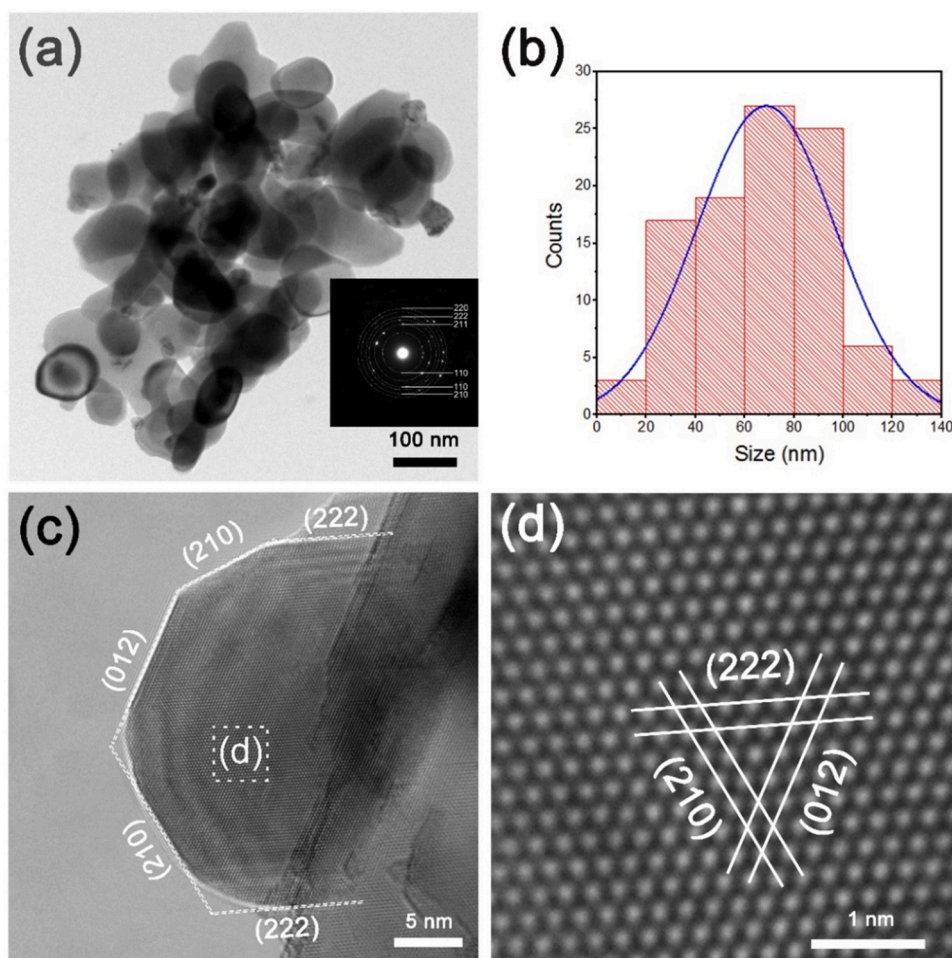


Fig. 5. (a) Typical BF TEM image of CTO NPs. Inset shows the corresponding SAED patterns. (b) Statistical size distribution of CTO NPs. (c) HRTEM image of an individual CTO nanoparticle. (d) Enlarged HRTEM image of the regions enclosed by white rectangles in (c).

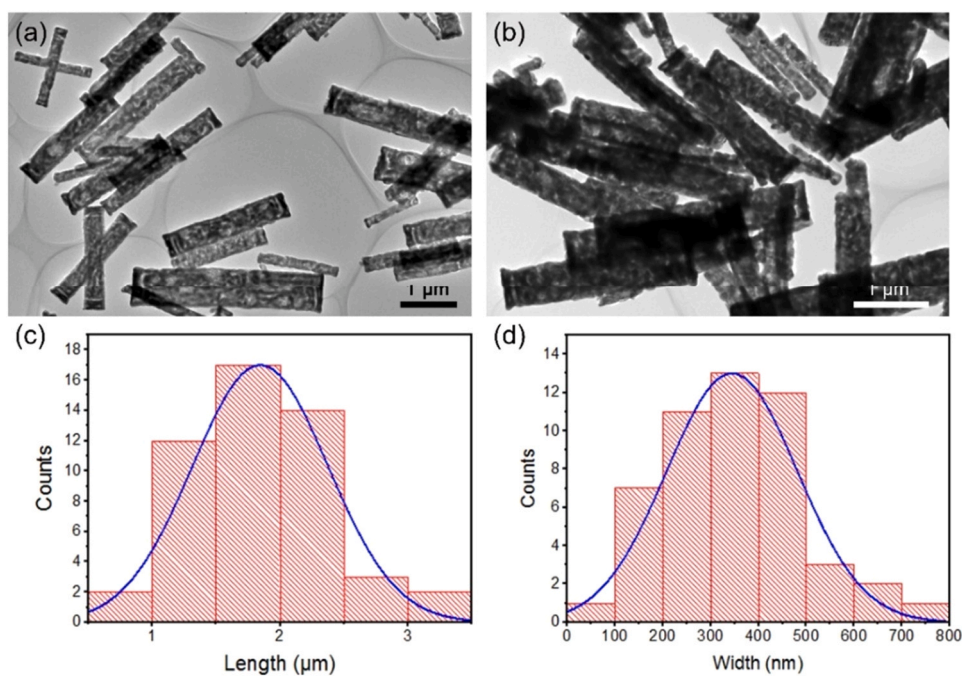


Fig. 6. (a, b) BF TEM images of CTO MRs. Statistical distributions of length (c) and width (d) of CTO MRs.

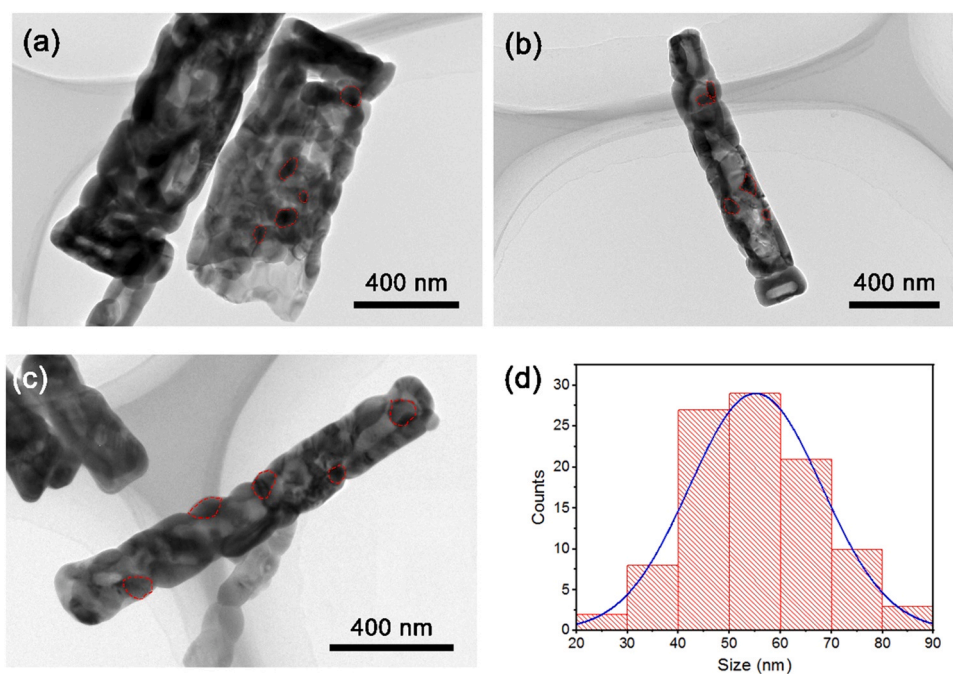


Fig. 7. (a, b, c) BF TEM images of CTO MRs. The part surrounded by the red dotted lines indicates nanoparticles on CTO MRs. (d) Statistical size distribution of nanoparticles on CTO MRs.

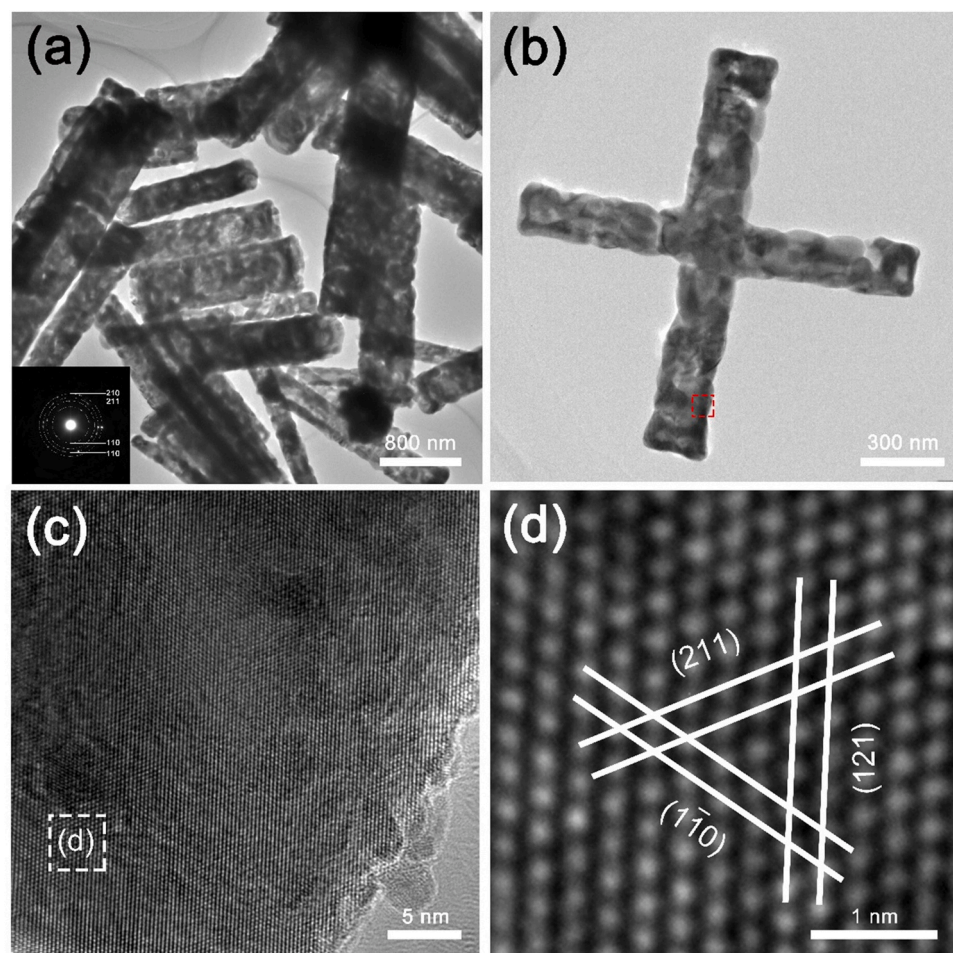


Fig. 8. (a) Typical BF TEM image of CTO MRs. Inset shows the corresponding SAED patterns. (b) TEM image of two cross rods. (c) Enlarged HRTEM image of the regions enclosed by red rectangles in (b). (d) Enlarged HRTEM image of the regions enclosed by white rectangles in (c).

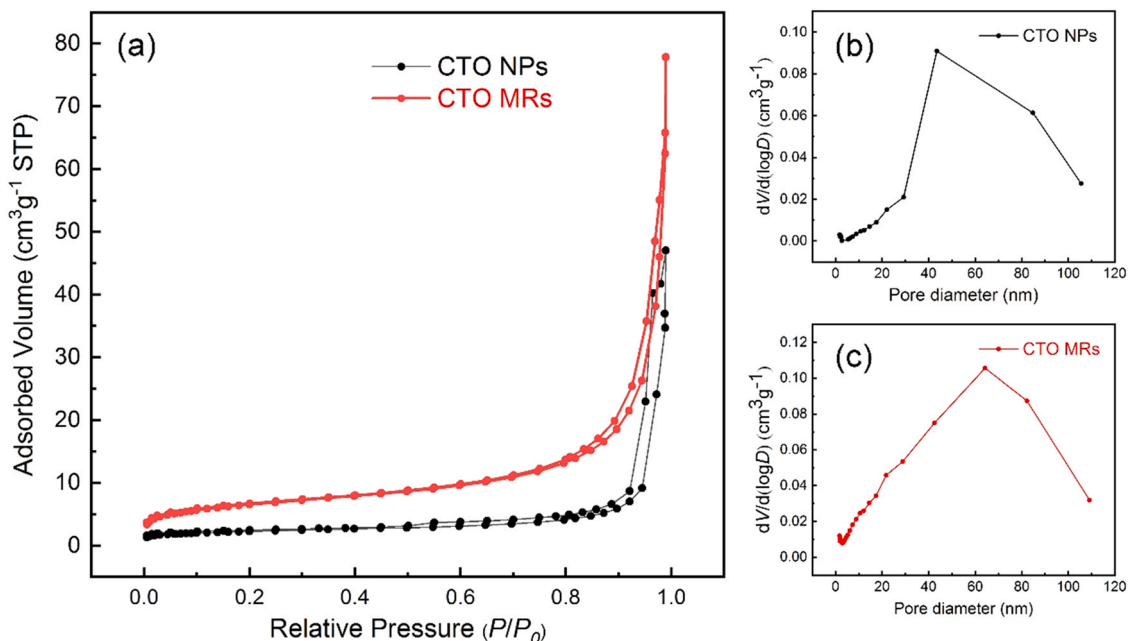
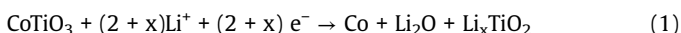


Fig. 9. (a) Nitrogen adsorption/desorption isotherms of CTO NPs and CTO MRs. Pore size distribution curves of the (b) CTO NPs and (c) CTO MRs.

average pore size of 45 nm and 65 nm, respectively. The total pore volumes of the CTO NPs and CTO MRs are 0.057 and 0.097 cm³ g⁻¹, respectively. The Brunauer–Emmett–Teller (BET) surface areas of CTO NPs and CTO MRs are calculated to be 7.49 and 15.11 m² g⁻¹, respectively. Due to the large specific surface area, CTO MRs promote the diffusion of Li⁺ in the electrode and keep the effective contact between electrode and electrolyte, and simultaneously provide more active sites for the storage of Li⁺, which can greatly enhance the lithium storage capacity [25].

To evaluate the electrochemical properties, the as-synthesized CTO NPs and CTO MRs are tested as anode materials for LIBs. Fig. 10a shows the CV curves of CTO NPs electrode in the 0.01–3.00 V voltage range at a scan rate of 0.3 mV s⁻¹. In the first cathode scan, there are two reduction peaks at 0.2 V and 0.9 V, due to the formation of solid electrolyte interface (SEI) film on the electrode [26]. In the subsequent electrochemical cycle, two reduction peaks at 1.8 V and 0.5 V might be related to the transformations from Co²⁺ and Ti⁴⁺ (in CTO) into Co⁰ and Ti³⁺, which is described by Eq. (1) [27].



A pair of reduction and oxidation peaks at 0.5 V and 2.3 V were caused by the mutual transformation of Co⁰ and Co²⁺. A pair of TiO₂ peaks were observed at about 1.8 V and 1.4 V, due to the insertion and extraction process of Li⁺ in titanium dioxide [28]. The electrochemical reactions can be summarized as follows.



Fig. 10b shows the CV curves of the first six cycles of CTO MRs electrode with a voltage range of 0.01–3.00 V. The position of the redox peak shown in the CV curves of the CTO MRs electrode is roughly the same as that of the CTO NPs electrode. The main difference is the intensity of the diffraction peak, which may be due to the larger overall size of CTO MRs than CTO NPs.

To investigate the cycling performance, two electrodes were tested for 200 cycles at a current density of 100 mA g⁻¹ (Fig. 10c). Due to the severe volume expansion of electrode materials, the

discharge specific capacity of the CTO NPs electrode gradually decreases and maintains only 245 mAh g⁻¹ after 200 cycles, resulting in inferior cycling stability. By contrast, the specific capacity of the CTO MRs electrode decreases to 362 mAh g⁻¹ for the 8th cycle, whereas it increases significantly to 503 mAh g⁻¹ for the 102nd cycle. Then it gradually drops, and finally is stabilized to 440 mAh g⁻¹ after 200 cycles. Due to the formation of an organic polymer gel-like layer arising from the incomplete decomposition of the electrolyte, the specific capacity decreases in the initial several cycles. Then the specific capacity increases significantly, which can be attributed to the following reasons. Firstly, the organic polymer gel-like layer could provide excess active sites for lithium storage [29–31]. Secondly, the activation of electrode materials (CTO MRs) after several cycles may lead to an improvement of specific capacity [29–31]. In addition, the porous characteristic of CTO MRs is beneficial for increasing the contact area between the electrode and electrolyte, and the one-dimensional structure helps to accommodate the volume change and thus maintains structural stability during the repeated discharge/charge process.

The rate capability of two electrodes was tested at different current densities of 0.1, 0.2, 0.5, 1 and 2 A g⁻¹, as shown in Fig. 9c. Compared with CTO NPs, the CTO MRs electrode exhibits a better rate capability with an average discharge capacity of 503, 353, 283, 212 and 171 mAh g⁻¹ at 0.1, 0.2, 0.5, 1 and 2 A g⁻¹, respectively. When the current density returns to 0.1 A g⁻¹, the discharge capacity of the CTO MRs electrode reaches 478 mAh g⁻¹ after 80 cycles, far higher than that of CTO NPs (302 mAh g⁻¹). This shows that the CTO MRs electrode has better rate performance. The porous structure with large specific surface area enables full contact between electrode and electrolyte, which is conducive to the transfer of lithium ions and electrons, thereby improving the electrochemical performance.

EIS measurements were carried out to explore the electrochemical reaction kinetics of both CTO NPs and CTO MRs electrodes in detail. Fig. 11 presents the EIS spectra of CTO NPs and CTO MRs electrodes before cycling. The spectra consist of a semicircle and a straight line, corresponding to high and low frequency regions, respectively. In the high frequency region, the semicircle diameter of CTO MRs electrode is smaller than that of CTO NPs, which suggests that CTO MRs have lower contact and charge transfer impedance. Furthermore, the inclined line at the low frequency region indicates

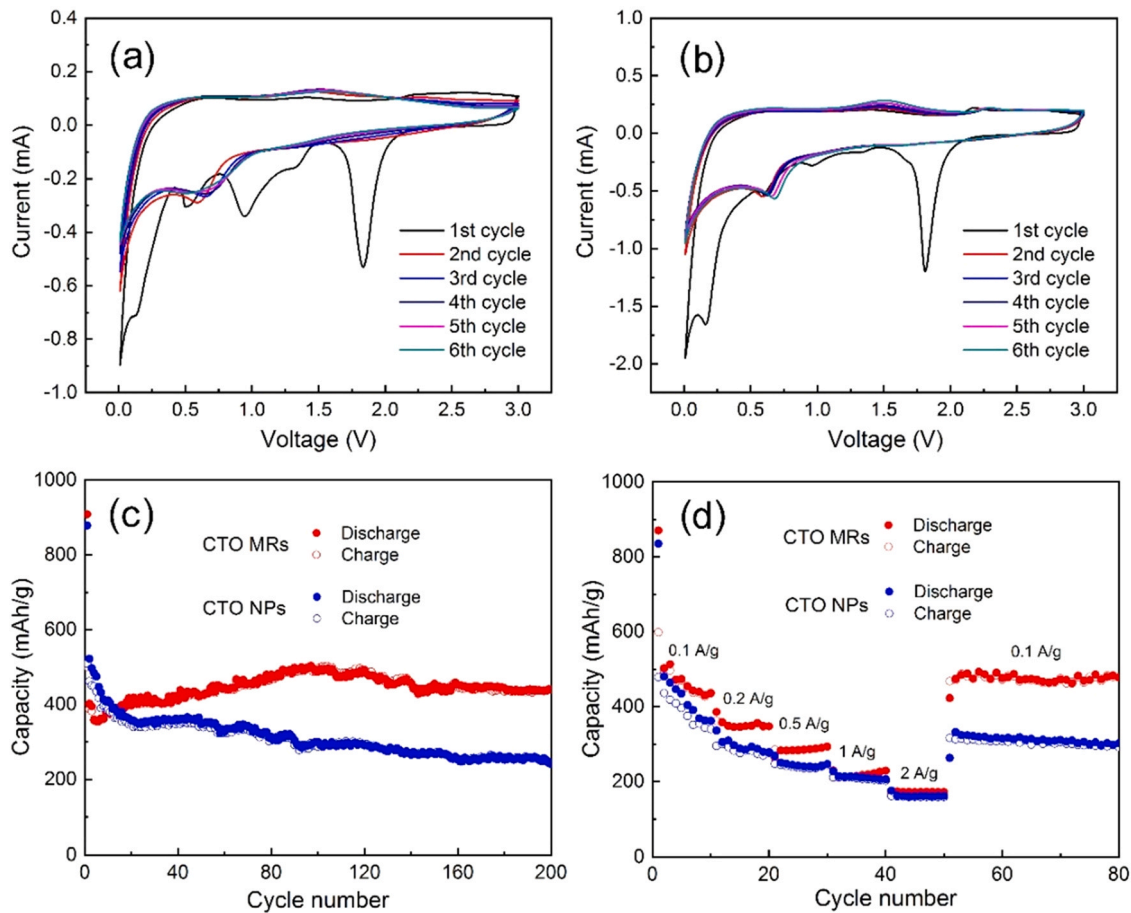


Fig. 10. CV curves of CTO NPs (a) and CTO MRs (b) electrodes at a scan rate of 0.3 mV s^{-1} . (c) Cycling performance of CTO MRs and CTO NPs electrodes at a current density of 100 mA g^{-1} . (d) Rate performance of CTO MRs and CTO NPs electrodes at various current densities.

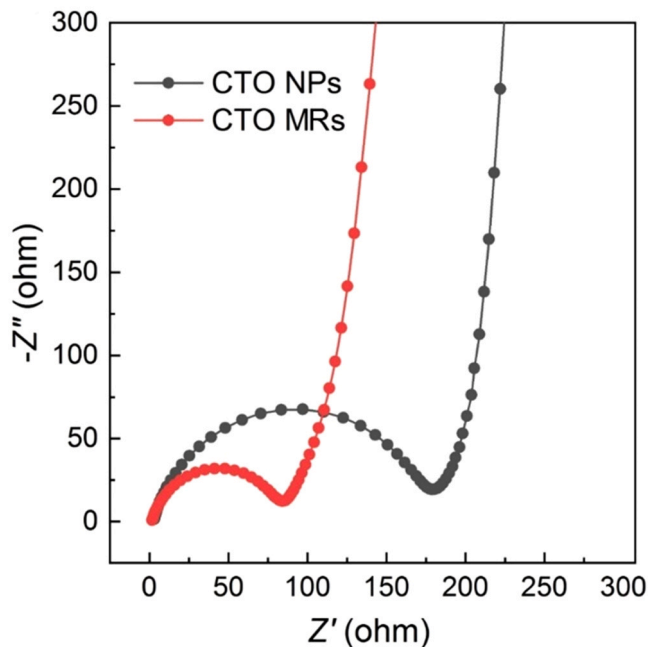


Fig. 11. EIS spectra of CTO NPs and CTO MRs electrodes before cycling.

that the capacitive-like behavior dominates in the CTO NPs and CTO MRs electrodes. The diffusion coefficient (D_{Li}) was calculated using the following equations [32].

$$D_{\text{Li}} = \frac{R^2 T^2}{2A^2 n^4 F^4 C^2 \sigma^2} \quad (4)$$

$$C = \frac{n}{V} = \frac{m/M}{V} \quad (5)$$

$$Z_{re} = R_s + R_{ct} + \sigma \omega^{-0.5} \quad (6)$$

where the constant values of F and R are $96,485 \text{ C mol}^{-1}$ and $8.314 \text{ J K}^{-1} \text{ mol}^{-1}$, respectively. A is the electrode area ($1.54 \times 10^{-4} \text{ m}^2$), n is the number of the electrons per molecule attending the electronic transfer reaction, T is 298.17 K , and C is calculated to be $1.07 \times 10^4 \text{ mol m}^{-3}$ from formula (5).

Fig. 12 shows the graph of Z_{re} plotted against $\omega^{-0.5}$. The σ values of CTO NPs and CTO MRs electrodes are determined to be 57.9 and $42.2 \Omega \text{ s}^{-0.5}$, respectively. The Li^+ diffusion coefficients of CTO NPs and CTO MRs electrodes are calculated to be 2.4×10^{-16} and $4.6 \times 10^{-16} \text{ cm}^2 \text{ s}^{-1}$, indicating that CTO MRs electrode exhibits better ionic diffusion ability compared to CTO NPs. We conclude that the porous structure of CTO MRs better promotes the diffusion path of Li^+ and accelerate electron transfer.

To elucidate the electrochemical process more clearly, CTO MRs and CTO NPs electrodes (after 200 cycles at 100 mA g^{-1}) were characterized by XRD. As shown in Fig. 13, the diffraction peaks can be indexed using the TiO_2 phase (JCPDS no.: 75–1750), Co phase (JCPDS no.: 89–4307) and CoO phase (JCPDS no.: 89–2803). The peak at 32.17° can be assigned to the (100) plane of CoO. The peak at 44.23° corresponds to the (111) plane of Co. The peaks at 36.08° , 54.32° and 64.05° correspond to the (101), (211) and (310) planes of TiO_2 . These results indicate that the transformation from Co^{2+} and Ti^{4+} (in CTO)

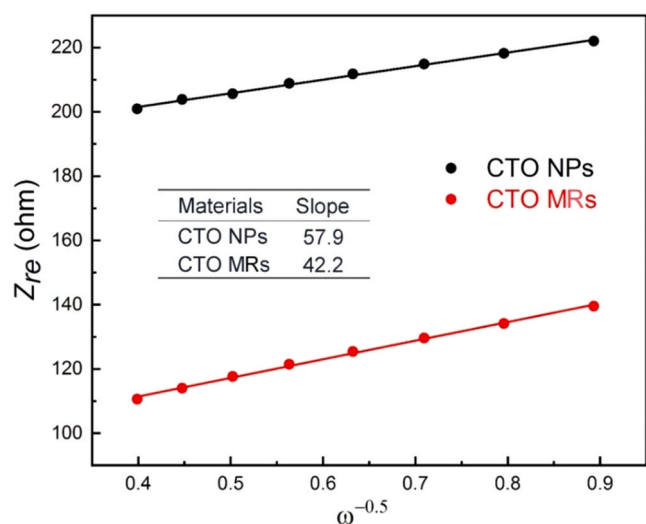


Fig. 12. Graph of Z_{re} plotted against $\omega^{-0.5}$.

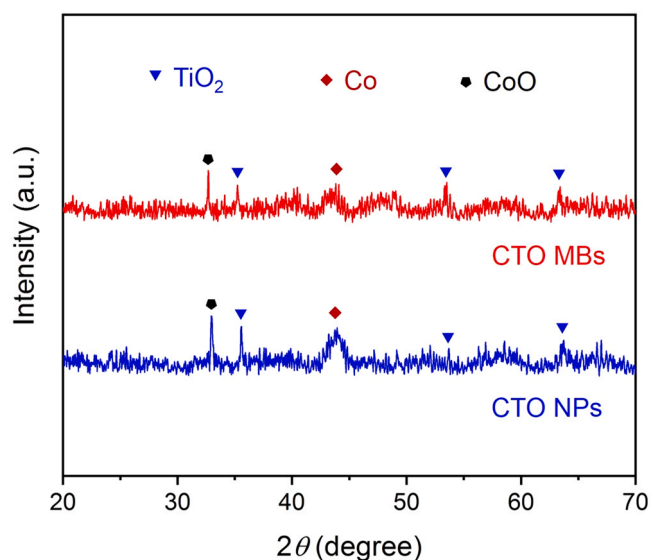


Fig. 13. XRD patterns of CTO MRs and CTO NPs electrodes after 200 cycles at a current density of 100 mA g^{-1} .

into Co^0 and Ti^{3+} occurs during the electrochemical process, as supported by CV curves (Fig. 10a).

4. Conclusions

In summary, CTO MRs and CTO NPs were prepared using a sample one-step solvothermal method followed by post-annealing. We then studied in depth the relationship between structure and electrochemical properties of both CTO NPs and CTO MRs. When evaluated as anode material for LIBs, the porous rod-like structure of CTO MRs buffers the volume expansion during the repeated Li^+ insertion/extraction process, and simultaneously improves the kinetic diffusion of Li^+ and electrons. The CTO MRs electrode shows a superior discharge capacity (410 mAh g^{-1} at 100 mA g^{-1} after 200 cycles) and better rate capacity, higher than that of CTO NPs. The porous structure is beneficial to reduce the agglomeration of CTO MRs and increase the contact area with the electrolyte, leading to a short diffusion path and facilitating the rapid transport of lithium ions/electrons. Our results suggest that the design of porous microstructure can achieve outstanding electrochemical performance

for LIBs and provide a feasible strategy to obtain high-performance LIBs.

CRedit authorship contribution statement

Meng Sun: Data curation, Formal analysis, Investigation, Validation, Visualization, Writing – original draft, Writing – review & editing. **Xiaoli Sheng:** Formal analysis, Validation, Visualization. **Tao Li:** Formal analysis, Validation. **Sijie Li:** Formal analysis, Validation. **Zhipeng Cui:** Formal analysis, Validation. **Qingye Zhang:** Formal analysis. **Fei Xie:** Validation. **Yiqian Wang:** Conceptualization, Funding acquisition, Resources, Supervision, Writing – review & editing.

Data availability

No data was used for the research described in the article.

Declaration of Competing Interest

The authors declare that they have no known competing financial interests or personal relationships that could have appeared to influence the work reported in this paper.

Acknowledgements

We would like to thank the financial support from the National Natural Science Foundation of China (Grant No.: 10974105), Shandong Province “Double-Hundred Talent Plan” Program (Grant No.: WST2018006), High end foreign experts project of the Ministry of Science and Technology (Grant no.: G2022025015L, G2022025016L). Y.Q. Wang would also like to thank the financial support from the Taishan Scholar Program, and Qingdao International Center for Semiconductor Photoelectric Nanomaterials and Shandong Provincial University Key Laboratory of Optoelectrical Material Physics and Devices.

References

- [1] K.H. Kim, S.H. Hong, Manganese tetraphosphide (MnP_4) as a high capacity anode for lithium-ion and sodium-ion batteries, *Adv. Energy Mater.* 11 (2021) 2003609.
- [2] Y.Y. Zhang, P. Chen, Q.Y. Wang, Q. Wang, K. Zhu, K. Ye, G.L. Wang, D.X. Cao, J. Yan, Q. Zhang, High-capacity and kinetically accelerated lithium storage in MoO_3 enabled by oxygen vacancies and heterostructure, *Adv. Energy Mater.* 11 (2021) 2101712.
- [3] F.H. Liang, D.N. Wu, L. Jiang, Z. Zhang, W. Zhang, Y.C.A. Rui, B.H.J. Tang, F.J. Liu, Layered niobium oxide hydrate anode with excellent performance for lithium-ion batteries, *ACS Appl. Mater. Interfaces* 13 (2021) 51057–51065.
- [4] S.Y. Wan, Q.M. Liu, M. Cheng, Y.C. Chen, H.Y. Chen, Binary-metal Mn_2SnO_4 nanoparticles and Sn confined in a cubic frame with N-doped carbon for enhanced lithium and sodium storage, *ACS Appl. Mater. Interfaces* 13 (2021) 38278–38288.
- [5] S.H. Wu, Y. Qi, W. Shi, M. Kuss, S.J. Chen, B. Duan, Electrospun conductive nanofiber yarns for accelerating mesenchymal stem cells differentiation and maturation into Schwann cell-like cells under a combination of electrical stimulation and chemical induction, *Acta Biomater.* 139 (2022) 91–104.
- [6] Y.H. Li, H. Sun, X.P. Cheng, Y.F. Zhang, K.J. Zhao, In-situ TEM experiments and first-principles studies on the electrochemical and mechanical behaviors of $\alpha\text{-MoO}_3$ in Li-ion batteries, *Nano Energy* 27 (2016) 95–102.
- [7] C.Y. Zhao, J.H. Kong, X.Y. Yao, X.S. Tang, Y.L. Dong, S.L. Phua, X.H. Lu, Thin MoS_2 nanoflakes encapsulated in carbon nanofibers as high-performance anodes for lithium-ion batteries, *ACS Appl. Mater. Interfaces* 6 (2014) 6392–6398.
- [8] K. Chang, W.X. Chen, L-cysteine-assisted synthesis of layered MoS_2 /graphene composites with excellent electrochemical performances for lithium ion batteries, *ACS Nano* 5 (2011) 4720–4728.
- [9] F.Y. Diao, Y.Q. Wang, Transition metal oxide nanostructures: premeditated fabrication and applications in electronic and photonic devices, *J. Mater. Sci.* 319 (2018) 28–33.
- [10] J. Liu, T. Li, H. Zhang, W.W. Zhao, L.J. Qu, S.J. Chen, S.H. Wu, Electrospun strong, bioactive, and bioabsorbable silk fibroin/poly (L-lactic-acid) nanoyarns for constructing advanced nanotextile tissue scaffolds, *Mater. Today Biol.* 14 (2022) 100243.
- [11] C. Liang, J.F. Chen, K.F. Yu, W.M. Jin, ZnMn_2O_4 spheres anchored on jute porous carbon for use as a high-performance anode material in lithium-ion batteries, *J. Alloy. Compd.* 878 (2021) 160445.

- [12] C.F. Zhang, G. Park, B.J. Lee, L. Xia, H. Miao, J.L. Yuan, J.S. Yu, Self-templated formation of fluffy graphene-wrapped Ni_5P_4 hollow spheres for Li-ion battery anodes with high cycling stability, *ACS Appl. Mater. Interfaces* 13 (2021) 23714–23723.
- [13] B. Xiao, G. Wu, T.D. Wang, Z.G. Wei, Y.W. Sui, B.L. Shen, J.Q. Qi, F.X. Wei, J.C. Zheng, High-entropy oxides as advanced anode materials for long-life lithium-ion batteries, *Nano Energy* 95 (2022) 106962.
- [14] W.W. Li, Q.B. Ma, P.F. Shen, Y.C. Zhou, L. Soule, Y.Y. Li, Y.X. Wu, H.Y. Zhang, M.L. Liu, Yolk-shell structured CuSi_2P_3 @Graphene nanocomposite anode for long-life and high-rate lithium-ion batteries, *Nano Energy* 80 (2021) 105506.
- [15] K. Chen, Y. Tan, K. Wang, J. Niu, Z.Y. Chen, High specific capacity of carbon coating lemon-like SiO_2 hollow spheres for lithium-ion batteries, *Electrochim. Acta* 401 (2022) 139497.
- [16] B.C. Sekhar, P. Packiyalakshmi, N. Kalaiselvi, Synergistic effect of flakes containing interconnected nanoparticles and conducting graphene additive to qualify ZnMn_2O_4 as potential lithium-battery anode, *Chemelectrochem* 4 (2017) 1154–1164.
- [17] J.K. Li, D. Wang, J.S. Zhou, L. Hou, F.M. Gao, MOF-derived in situ synthesized carbon-coated ilmenite cobalt titanate nanocrystalline, high-stability lithium-ion batteries, *J. Alloy. Compd.* 793 (2019) 247–258.
- [18] Y. Qu, W. Zhou, H.G. Fu, Porous cobalt titanate nanorod: a new candidate for visible light-driven photocatalytic water oxidation, *Chemcatchem* 6 (2014) 265–270.
- [19] Y.W. Tang, L.J. Wu, L. Xiao, D.Q. Wen, Q.W. Guo, W.C. Liang, Porous CoTiO_3 microbars as super rate and long life anodes for sodium ion batteries, *Ceram. Int.* 44 (2018) 18025–18031.
- [20] E.S. Kim, C.J. Jeon, Microwave dielectric properties of ATiO_3 (A = Ni, Mg, Co, Mn) ceramics, *J. Eur. Ceram. Soc.* 30 (2010) 341–346.
- [21] J.J. Zou, B. Liu, H.Q. Liu, Y.H. Ding, T. Xin, Y.Q. Wang, Facile synthesis of interconnected mesoporous ZnMn_2O_4 nano-peanuts for Li-storage via distinct structure design, *Mater. Res. Bull.* 107 (2018) 468–476.
- [22] Z.P. Cui, M. Sun, H.Q. Liu, S.J. Li, Q.Y. Zhang, C.P. Yang, G.J. Liu, J.Y. Zhong, Y.Q. Wang, Double-shell SnO_2 @ Fe_2O_3 hollow spheres as a high-performance anode material for lithium-ion batteries, *Crystengcomm* 22 (2020) 1197–1208.
- [23] S.J. Li, J.Y. Zhong, Z.P. Cui, Q.Y. Zhang, M. Sun, Y.Q. Wang, Electron beam-induced morphology transformations of Fe_2TiO_5 nanoparticles, *J. Mater. Chem. C* 7 (2019) 13829–13838.
- [24] Z. Zhang, Y. Huang, X.D. Liu, X. Wang, P.B. Liu, c, Yolk-shell structured ZnCo_2O_4 spheres anchored on reduced graphene oxide with enhance lithium/sodium storage performance, *Electrochim. Acta* 342 (2020) 136104.
- [25] M. Madian, L. Giebeler, M. Klose, T. Jaumann, M. Uhlemann, A. Gebert, S. Oswald, N. Ismail, A. Eychmuller, J. Eckert, Self-organized TiO_2 /CoO nanotubes as potential anode materials for lithium ion batteries, *ACS Sustain. Chem. Eng.* 3 (2015) 909–919.
- [26] H. Liu, X.N. Wu, E.Y. Guo, Q.F. Lu, Tailored synthesis of coral-like CoTiO_3 / Co_3O_4 / TiO_2 nanobelts with superior lithium storage capability, *Energy Technol.* 8 (2020) 1900774.
- [27] X. Yang, Y. Wang, Y.Y. Hu, H.S. Zhao, Y.Y. Sun, K. Hua, G. Chen, Interior supported hierarchical TiO_2 @ Co_3O_4 derived from MOF-on-MOF architecture with enhanced electrochemical properties for lithium storage, *Chemelectrochem* 6 (2019) 3657–3666.
- [28] J. Wang, J. Polleux, J. Lim, B. Dunn, Pseudocapacitive contributions to electrochemical energy storage in TiO_2 (anatase) nanoparticles, *J. Phys. Chem. C* 111 (2007) 14925–14931.
- [29] B.X. Ouyang, T. Chen, R. Qin, P.G. Liu, X.W. Fan, J. Wang, W.F. Liu, K.Y. Liu, Bimetal-organic-framework derived CoTiO_3 /C hexagonal micro-prisms as high-performance anode materials for metal ion batteries, *Mater. Chem. Front.* 5 (2021) 5760–5768.
- [30] X. Wang, W.J. Cheng, J.Q. Hu, Y. Su, X.G. Kong, S. Uemura, T. Kusunose, Q. Feng, Lithium ion battery anode of mesocrystalline CoTiO_3 / TiO_2 nanocomposite with extremely enhanced capacity, *ACS Appl. Energy Mater.* 4 (2021) 13646–13656.
- [31] S.Y. Liu, C.Y. Fan, H.C. Wang, J.P. Zhang, X.L. Wu, Electrochemical in situ formation of a stable Ti-based skeleton for improved Li-storage properties: a case study of porous CoTiO_3 nanofibers, *Chem. Eur. J.* 23 (2017) 8712–8718.
- [32] X.L. Sheng, T. Li, M. Sun, G.J. Liu, Q.Y. Zhang, Z.B. Ling, S.W. Gao, F.Y. Diao, J.Z. Zhang, F. Rosei, Y.Q. Wang, Flexible electrospun iron compounds/carbon fibers: phase transformation and electrochemical properties, *Electrochim. Acta* 407 (2022) 139892.